

# Steady and Unsteady Numerical Simulation of a Bent Intake Geometry

Thomas Kächele, Tim Schneider and Reinhard Niehuis

**Abstract** A broad range of numerical flow simulations are carried out during the design phase of a highly bent intake geometry. The main aim is to evaluate the aerodynamic characteristics of a projected wind tunnel model and an estimation of mechanical loads for the structural dimensioning. The numerical setup using the TRACE code is validated first against comprehensive experimental data of a NASA s-duct test case. Three different turbulence models are found to be capable of reproducing the main flow features that occur in bent intake ducts with an acceptable accuracy. The following steady simulations of the symmetric wind tunnel model show asymmetric flow solutions and convergence problems for two of the three turbulence models. URANS computations are therefore carried out including a sensitivity study towards time-step size and domain volume. The unsteady results using the three different turbulence models still exhibit significant deviations concerning mechanical loads and duct performance. A safety margin is thus estimated from the unsteady data to be used for the construction and testing of the wind tunnel model.

## 1 Introduction

Modern aircraft concepts feature complex engine intake configurations for various reasons. The reduction of aircraft drag through boundary layer ingestion motivates the development of such civil configurations, a low observability by means of hiding the highly reflective fan plane of the jet engine lies in the focus of military applications. These unconventional intake geometries result in a disturbed flow regime towards the compression system of the jet engine. The consequences are

---

T. Kächele (✉) · R. Niehuis  
Institute of Jet Propulsion, Universität der Bundeswehr München,  
Werner-Heisenberg-Weg 39, 85577 Neubiberg, Germany  
e-mail: thomas.kaechele@unibw.de

T. Schneider  
MTU Aero Engines AG, Dachauer Str. 665, 80995 Munich, Germany  
e-mail: Tim.Schneider@mtu.de

© Springer International Publishing AG 2018

A. Dillmann et al. (eds.), *New Results in Numerical and Experimental Fluid Mechanics XI*, Notes on Numerical Fluid Mechanics and Multidisciplinary Design 136, [https://doi.org/10.1007/978-3-319-64519-3\\_2](https://doi.org/10.1007/978-3-319-64519-3_2)

performance deficits and a reduced stability margin. The generated flow distortion within the aerodynamic interface plane (AIP) between intake and engine is both dependent on the duct geometry as well as the upstream influence of the compressor. In order to improve the knowledge about this interaction and to validate different simulation approaches, a highly bent intake geometry was developed for an experimental investigation in cooperation with MTU Aero Engines AG [1]. Experiments will take place in the engine test facility of the Institute of Jet Propulsion at the University of the German Federal Armed Forces in Munich featuring the MexJET test engine [2]. During the iterative design process, numerical flow simulations were carried out for two reasons. The first is the prediction and evaluation of the resulting distortion pattern to achieve a significant AIP flow distortion without the risk of compressor surge. The second reason is an estimation of the expected wall pressure distribution to simulate the mechanical loads on the duct as well as on the support structure. As the simulation of highly contoured intake geometries by means of RANS calculations is very challenging, an estimation of numerical uncertainty and thus an additional safety margin for the load cases was necessary.

## 2 Intake Aerodynamics

During the design phase of the duct, no best practice setup for the simulation of intake ducts with the flow solver TRACE was available. The numerical settings were therefore calibrated using comprehensive experimental data generated by a NASA test campaign of a comparable single s-bent duct by Wellborn and Okiishi [3]. This geometry is compared to the MexJET duct in Fig. 1. The NASA duct on the left side

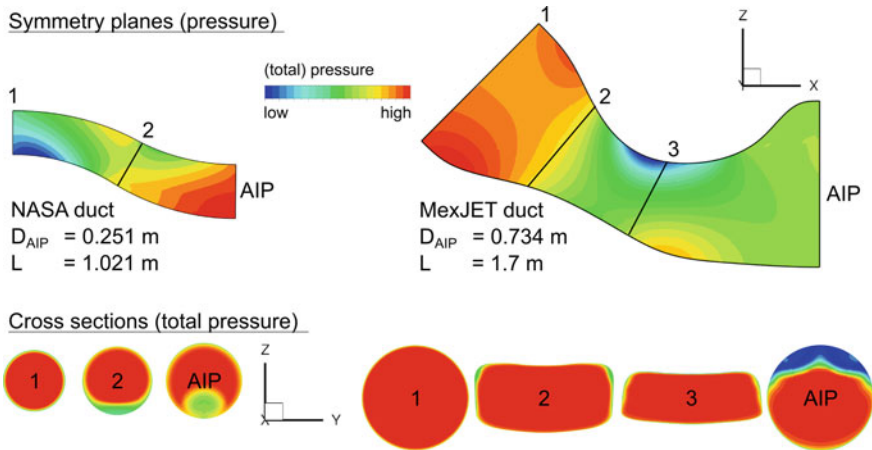


**Fig. 1** Comparison of NASA duct (left) and MexJET duct (right) with pressure values in the symmetry plane and total pressure values in different cross sections in the same scale

features circular cross sections which are constantly increasing in area leading to an area ratio  $A_{AIP}/A_1$  of 1.52. The MexJET duct geometry on the right has a circular inlet (Sect. 1) that transforms to a nearly rectangular shape (Sect. 3) while cross-sectional area decreases to  $A_3/A_1 = 0.78$ . From this throat, the geometry changes to a circular outlet with  $A_{AIP} = A_1$ .

As the flow passes through the duct, changes in centerline curvature and cross-sectional area lead to a complex static pressure field. The upper half of Fig. 1 shows the respective symmetry plane of both ducts. In case of the NASA duct, a cross-stream pressure gradient exists within the first bend between Sects. 1 and 2 with higher pressure at the top wall ( $\phi = 0^\circ$ ) and lower pressure on the bottom wall ( $\phi = 180^\circ$ ). The gradient causes the formation of secondary flows and vortical structures that transport low momentum boundary layer fluid towards the bottom of the duct. This is clearly visible within the total pressure distribution in Sect. 2. An adverse streamwise pressure gradient around the bottom of cross Sect. 2 leads to a flow separation at the lower wall. A further convection of low momentum boundary layer fluid towards the center of the duct through a pair of counter-rotating tornado-like vortices takes place within the second bend. As a result, the AIP shows swirl as well as a static and total pressure distortion.

In order to quantify the complex AIP flow patterns, performance parameters are used. Examples are the total pressure ratio  $\Pi_t$  and the total pressure distortion coefficient  $DC60$  [4, 5] (cf. Eq. 1). The latter compares the average total pressure within the strongest distorted  $60^\circ$  segment  $\bar{p}_{t,60}$  with the mean total pressure of the entire plane  $\bar{p}_{t,AIP}$ . The difference is then nondimensionalized by the dynamic AIP pressure  $\bar{q}_{AIP}$ . Within this paper, spatial averages are obtained by a flux averaging while a simple arithmetic averaging is used for temporal averages.

$$\Pi_t = \frac{P_{t,AIP}}{P_{t,1}}, \quad DC60 = \frac{\bar{p}_{t,AIP} - \bar{p}_{t,60}}{\bar{q}_{AIP}} \quad (1)$$

The experimental data from the NASA case comprise static wall pressure at three circumferential positions along the duct ( $\phi = 10^\circ, 90^\circ, 170^\circ$ ) as well as static and total pressure measurements in five cross-sectional planes. For the calculation of the dimensionless coefficients,  $c_p$  and  $c_{p,t}$ , reference data from an inlet plane control point is applied.

$$c_p = \frac{p - p_{ref}}{p_{t,ref} - p_{ref}}, \quad c_{p,t} = \frac{p_t - p_{t,ref}}{p_{t,ref} - p_{ref}} \quad (2)$$

For an evaluation of the MexJET duct geometry, the precision of the simulation as well as its sensitivity towards modelling parameters is important. The mechanical loads on duct and support structure result from the pressure difference between inner and outer duct surface. The AIP total pressure distribution in terms of the  $DC60$  parameter on the other hand determines the safe operation of the experimental setup.

### 3 Validation of Numerical Setup

The numerical simulations presented within this paper were carried out using the turbomachinery research flow solver TRACE [6, 7] developed by the DLR Institute of Propulsion Technology in collaboration with MTU Aero Engines AG. This code solves the (unsteady) Reynolds-averaged Navier-Stokes equations with a finite volume approach on multi-block curvilinear meshes. Previous comparisons to experimental data of subsonic bent intake ducts by Brear et al. [8], or Gerolymos et al. [9] show the general suitability of RANS simulations featuring two-equation eddy-viscosity turbulence models to reproduce the main flow characteristics. Still, as AIP total pressure distributions are very sensitive to the prediction of upstream flow topologies, precise reproduction of the separation onset as well as the development and dissipation of vortex structures remains a challenging task.

For the following validation, only two characteristics of the NASA duct flow will be discussed. The first is the static wall pressure distribution along the bottom of the duct at  $\phi = 170^\circ$  as shown in Fig. 2. The experimental data show the adverse pressure gradient as well as the region of separated flow indicated by a pressure plateau between  $2.0 < s/d < 3.2$ . The other characteristic is the AIP total pressure distribution in Fig. 3. Boundary layer thicknesses as well as the further development of the total pressure distortion through the pair of counter-rotating vortices can be compared from this data.

The following parameters of the numerical setup were investigated: Grid resolution, wall resolution as well as transition and turbulence modelling. While experimental inflow conditions for total pressure, total temperature, Mach, and Reynolds number as well as turbulence intensity and boundary layer thicknesses are carefully

**Fig. 2** TRACE simulations of NASA case: static wall pressure coefficient at variation of inflow turbulent length scale for the  $k\text{-}\omega$ -SLC model

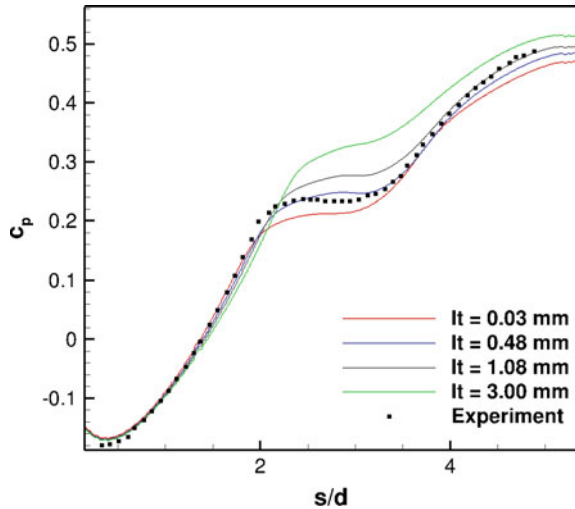
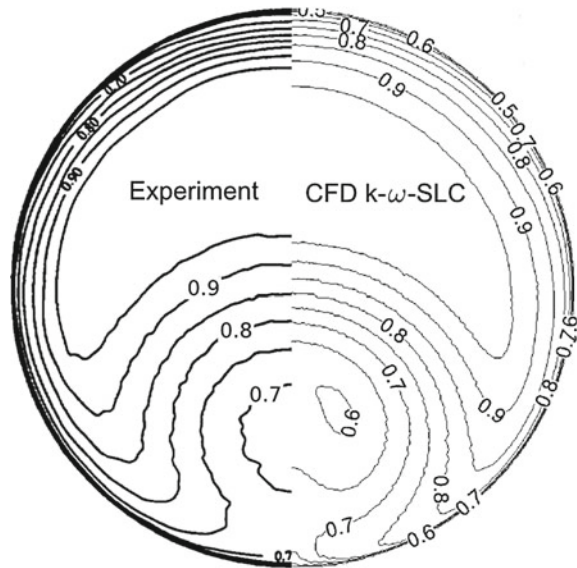


**Fig. 3** Comparison of TRACE simulations of NASA case featuring the  $k-\omega$ -SLC model and experimental result: total pressure coefficient at duct outlet



described by NASA no information was given concerning the inflow turbulent length scale. Thus, simulations with different length scales were also necessary.

### Computational Mesh

An initial mesh was created in a butterfly topology featuring 0.8 million cells and satisfying the criterion for the use of a low Reynolds wall formulation (non-dimensional height  $y^+$  of the wall closest cell below 1). This mesh was subsequently refined in all spatial directions up to a cell number of 52.8 million. Using a mesh with a cell number of 3.2 million resulted in deviations of  $\Delta DC60 = 2.5\%$  and  $\Delta \Pi_t = 0.1\%$  compared to the finest mesh flow solution. Regarding the intake design process, where a large number of duct geometries needs to be evaluated, this precision was accepted. Improvements through a further refinement did not justify the increase in calculation effort. A cell number of about 3–5 million is also recommended for this geometry by Delot and Scharnhorst [10] summarizing the results of the first AIAA Propulsion Aerodynamics Workshop (PAW01).

The boundary layer resolution of the final mesh was then coarsened (height of wall closest cell  $y^+ > 30$ ) and wall functions were applied. Using this mesh, wall pressures, secondary flows, and the separation location were predicted with a similar precision but a reduction of cell number by about 20%. Compared to the finest mesh, deviations of  $\Delta DC60 = 1.3\%$  and  $\Delta \Pi_t = 0.1\%$  arose for the wall function mesh.

### Turbulence Modelling

The inflow Reynolds number related to the inlet diameter is  $Re_{D_i} = 2.6 \cdot 10^6$ , therefore the flow can be considered fully turbulent. A variation of the turbulence modelling has the largest impact on the generation and the development of the vortex pair and thus the AIP flow distortion. Best results were achieved for a Wilcox  $k-\omega$  model

with an additional streamline curvature correction by Kozulovic and Röber [11] ( $k$ - $\omega$ -SLC), the Menter 2003 SST model [12] and an Explicit Algebraic Reynolds Stress Model (EARSM) [13]. The latter two models predict a more compact region of low total pressure in the AIP, causing increased DC60 values compared to the  $k$ - $\omega$ -SLC model and the experiment.

Variations of the inflow turbulent length scale reveal a very strong influence on the wall static pressures in the region of flow separation as shown in Fig. 2. With a suitable length scale (in this case  $l_t = 1.08$  mm), the computed curve fits the measured pressure distribution quite well while a smaller length scale leads to reduced wall pressures and thus increased pressure loads on the duct surface. Following this finding, additional measurement equipment for turbulent intensity was added to the experimental setup of the MexJET duct.

## 4 Steady MexJET Duct Simulations

Two meshes were generated for the MexJET duct using the mesh resolution identified by the NASA duct simulations. One mesh for a low Reynolds wall formulation and a coarser mesh using wall functions. Undisturbed inflow at ISA conditions ( $T_t = 288.15$  K,  $p_t = 101,325$  Pa) with a turbulence level of 5% were applied. The turbulent length scale was set to  $l_t = 0.3$  mm in order to increase numerical stability. The static outlet pressure was varied to achieve a constant inlet mass flow as it will occur during experimental testing. The selected Riemann boundary condition formulation dictates an constant static pressure at the domain outlet and suppresses any backflow. In order to eliminate the influence of the outlet boundary condition on the AIP flow field, the duct geometry was extended by a straight cylindrical tube with a length of  $dx = 1.7 \cdot D_{AIP}$ . Again, comparable results concerning wall pressure distribution and AIP total pressure were computed for the two meshes.

### Wall pressure distribution

While a variation of mesh resolution and wall treatment led to minor differences in wall pressure distribution, significant deviations arose for an application of the SST and EARSM turbulence model as shown in Fig. 4. All models predict the same development within the convergent part of the duct  $x/D_{AIP} < -1.1$ . In the following diffusing section, the adverse pressure gradient at the upper side of the duct ( $\phi = 0^\circ$ ) leads to a flow separation around  $x/D_{AIP} = -0.5$ . The values for the  $k$ - $\omega$ -SLC model indicate a later onset of the flow separation compared to SST and EARSM. Additionally, the first model shows higher wall pressures within the separated region. This suggests a larger aerodynamic cross section and thus a reduced extent of the flow separation. A comparison of the AIP total pressure plots in Fig. 5 confirms this assumption. Calculating the wall streamlines reflect a symmetric flow field and a separation line parallel to the AIP for the  $k$ - $\omega$ -SLC model. SST and EARSM results show an asymmetric separation location and AIP total pressure distribution.

**Fig. 4** Steady flow simulations: wall pressure coefficient at upper ( $0^\circ$ ) and lower ( $180^\circ$ ) wall of MexJET duct for different turbulence models

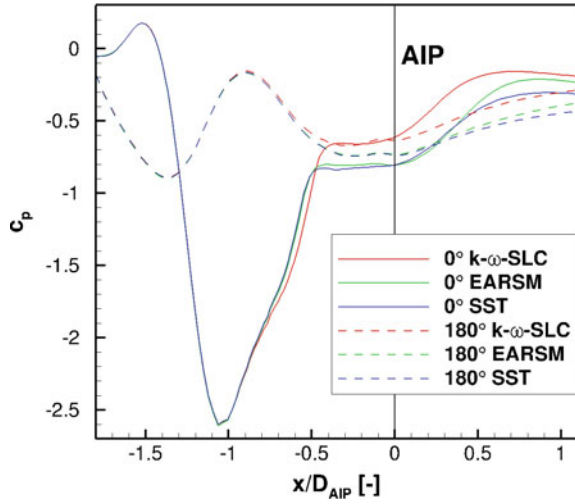
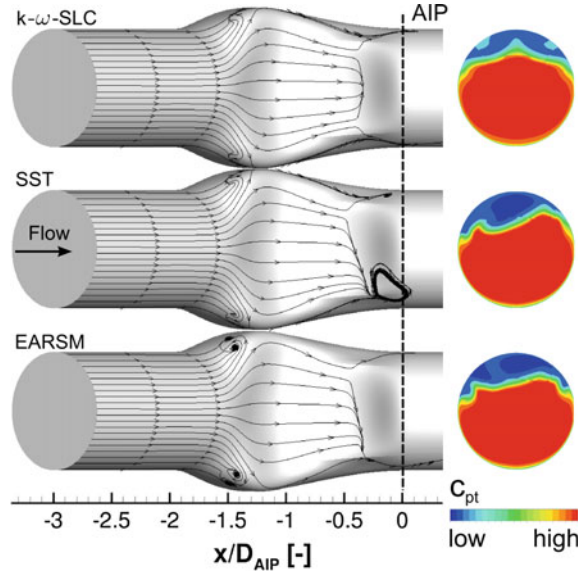


**Fig. 5** Steady flow simulations: wall stream lines on the upper side of the duct and AIP total pressure profiles for different turbulence models



### AIP flow field

The asymmetric flow fields calculated using SST and EARSIM model result in strongly differing DC60 values ( $k\text{-}\omega\text{-SLC}$  : 0.33,  $SST$  : 0.62 and  $EARSIM$  : 0.50). The steady simulation of this symmetric duct geometry is expected to result in a symmetric flow solution, even in case of an unsteady flow separation. As this unsteadiness turned out to be significantly strong, URANS simulations with all three turbulence models were undertaken.

## 5 Unsteady MexJET Duct Simulations

In URANS calculations, the temporal aspect of a flow field is resolved by a determined time-step  $\Delta t$ , where each time-step needs to be simulated by a number of sub-iterations. In analogy with a grid dependence study to identify the necessary spatial discretization, the required time-step size has to be evaluated by a time-step study. In a second study, the influence of the domain volume on the resulting unsteadiness was investigated. Finally, the results of the three turbulence models were compared concerning duct performance.

### Characteristic of unsteady duct flow field

The flow separation and its wake is an unsteady phenomenon which is dependent on the local kinetic energy of the fluid on the one side and the pressure gradient on the other. As the size of the flow separation is unsteady, the blockage and thus flow conditions (mass flow, pressure, velocities) close to the separation point vary as well. To quantify the impact of the parameter study, the following discussions include global performance and distortion parameters as well as unsteady probe data and an analysis of the dominant frequencies.

### Influence of time-step size and domain length

Unsteady simulations were carried out with time-step sizes ranging between 0.05 and 1.0 ms. Dependent on the time-step size, a varying number of sub-iterations per time-step is required for unsteady convergence (meaning a residual drop of 1.5 orders of magnitude in this case). It was found that the number of required sub-iterations decreases with a reduction of time-step size, such that a doubling of the temporal resolution only leads to an 50% increase of calculation effort. The number of sub-iterations as well as the computational effort in terms of a normalized simulation time is summarized in Table 1 for computations with the  $k\text{-}\omega$ -SLC model.

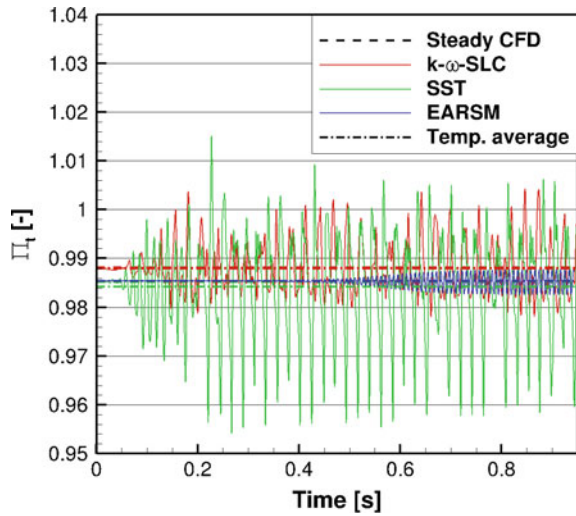
In all URANS simulations, the unsteady behavior of the flow separation leads to fluctuations of the flux averaged total pressure in the AIP. Both evaluated performance parameters,  $\Pi_t$  and  $DC60$ , are affected by the amplitudes and frequencies of these fluctuations. Results of all time-step sizes indicate increased amplitudes within a frequency band around 30–50 Hz as well as the higher harmonics at 60–90 Hz and 110–130 Hz. Compared to the high sampling frequency (1–20 kHz), the relatively low frequencies of the total pressure characteristic are captured by all used time-step sizes. However, larger (and thus coarser) time-step sizes lead to a damping of the calculated amplitudes. A time-step size of 0.1 ms was finally selected in order to

**Table 1** Required number of sub-iterations per time-step and normalized calculation time for varying time-step sizes

$\Delta t$ (ms)	Sub-iterations	Calculation effort
1.0	25	1.0
0.5	17	1.47
0.1	7	3.09
0.05	6	5.46



**Fig. 6** Unsteady AIP total pressure ratio and temporal average (*dash-dotted*) compared to the value of the steady simulation (*dashed line*) for different turbulence models



carry out all further calculations of the parameter study in a reasonable time frame. To investigate the influence of the volume of the calculation domain, the length of the extension of the cylindric tube  $dx$  at the duct outlet is varied. All simulations with  $dx > 1.5 \cdot D_{AIP}$  predict the first peak between 25 and 40 Hz. A boarder frequency range results for the harmonics, however no clear relation between  $dx$  and frequencies could be identified.

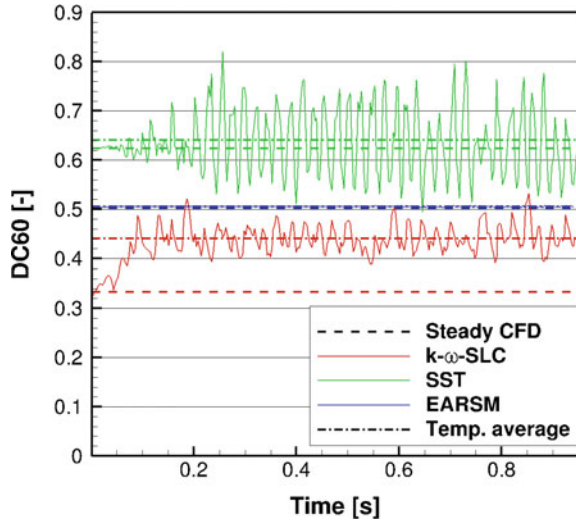
### Influence of turbulence modelling

Finally, unsteady flow solutions originating from the three mentioned turbulence models are compared. Three different flow solutions arose as it is depicted in terms of the transient performance parameters  $\Pi_t$  and DC60 in Figs. 6 and 7. While the  $k\omega$ -SLC and SST turbulence model show unsteady AIP total pressure levels with amplitudes of 1% and 2.5% respectively, the calculation featuring the EARSIM only shows a very weak unsteady behavior with a constant amplitude after 0.65 s of calculated time. Caused by mass flow fluctuations and backflow within the AIP due to the flow separation, pressure ratios  $\Pi_t > 1$  are calculated temporarily. The temporal average depicted as dash-dotted line, however, nearly perfectly aligns with the value of a steady flow solution (dashed lines).

The unsteadiness has an even stronger impact on the DC60 values. The SST results again show the largest fluctuations of up to 20% followed by the  $k\omega$ -SLC with a variation of 10%. While the temporal average of the SST flow solution is close to the value of the steady simulation, an increase by more than 30% is observed for simulations featuring the  $k\omega$ -SLC model.

The largest mechanical loads on the duct structure occur at the location of the lowest wall pressure at the upper side ( $\phi = 0^\circ$ ,  $x = -0.99$  cf. Fig. 4). Within the obtained unsteady data, the transient fluctuations of this pressure level stay below 5% for the  $k\omega$ -SLC model and rise to 9% regarding the SST model. A safety factor

**Fig. 7** Unsteady DC60 and temporal average (dash-dotted) compared to the value of the steady simulation (dashed line) for different turbulence models



of 10% on the local surface loads is considered for the structural analysis of the duct and the support structure to account for these variations due to different numerical parameters. An even higher safety margin is required for the AIP DC60 distortion parameter due to the detected uncertainties.

## 6 Conclusion and Outlook

During the design phase of a highly contoured intake geometry for experimental investigations, numerical flow simulations were used to predict intake performance and mechanical loads. No best practice setup was available for the used flow solver TRACE. Thus, a validation through experimental data originating from a NASA test campaign was carried out in advance. Three different turbulence models, an  $k$ - $\omega$ -SLC model, the Menter SST model, and an explicit algebraic Reynolds stress model (EARSM) were found to be capable of reproducing the main flow characteristics. The achieved accuracy was adequate for pre-test predictions. Applied on steady flow simulations of the contoured intake geometry, convergence problems and asymmetric flow solutions arose due to a strongly unsteady flow separation within the duct. During successive URANS computations, an adequate time-step size was found and an dependence on the volume of the simulated domain could be excluded. Still, the use of the three turbulence models led to diverging flow solutions. While the expected mechanical loads on the duct surface as a result of wall pressures could be handled by a safety margin of 10%, the predicted AIP total pressure distortion in terms of DC60 turned out to be very sensitive on the respective turbulence model. The occurring uncertainties point out the set-up and importance of a proper and comprehensive experimental test case which also features unsteady measurement equipment.

For an accurate representation of the intake flow field as it occurs during experiments, the turbulent inflow conditions need to be carefully captured as well. Therefore, additional measurement equipment is added to the experimental setup. Moreover, the influence of the engine compressor cannot be neglected as it will be located less than one AIP diameter downstream of the duct outlet. Preliminary coupled computations of duct and a low pressure compressor [14] show an influence on the static pressure field within the duct and thus the manipulation of secondary flows through the distorted compressor.

**Acknowledgements** These simulations were carried out within the frame of the COORETEC-Turbo 2020 project no. 1.2.4a. “Stabilität des Verdichtungssystems bei Off-Design Zuströmbedingungen”. This AG Turbo project is funded by the German Ministry of Economy and Technology (BMWi) and conducted in cooperation with MTU Aero Engines AG.

## References

1. Rademakers, R.P.M., Kächele, T., Niehuis, R.: Integration of a highly bent engine inlet in an engine test facility. In: Proceedings of ISROMAC Symposium of Rotating Machinery, Honolulu, USA, ISROMAC2016-112 (2016)
2. Bindl, S., Muth, B., Niehuis, R.: Adaption of a ground test facility to operate a modern turbo jet engine. In: Proceedings of the 21st International Symposium on Air Breathing Engines, Busan, Korea, ISABE-2013-1307 (2013)
3. Wellborn, S.R., Okiishi, T.H.: A study of the compressible flow through a diffusing S-duct. NASA Technical Memorandum 106411 (1993)
4. Society of Automotive Engineers: Gas turbine engine inlet flow distortion guidelines. Aerospace Recommended Practice 1420, Rev. B (2002)
5. Society of Automotive Engineers: Inlet total pressure considerations for gas turbine engines. Aerospace Information Report 1419, Rev. B (2013)
6. Nürnberger, D.: Implizite Zeitintegration für die Simulation von Turbomaschinenströmungen. Dissertation, DLR Forschungsbericht 2004-27 (2004)
7. Kügeler, E.: Numerisches Verfahren zur genauen Analyse der Kühleffektivität filmgekühlter Turbinenschaufeln. Dissertation, DLR Forschungsbericht 2005-11 (2005)
8. Brear, M.J., Warfield, Z., Magnus, J.F.: Flow separation within the engine inlet of an uninhabited combat air vehicle. In: Proceedings of FEDSM'03, 4th ASME Joint Fluids Engineering Conference, Honolulu USA (2003)
9. Gerolymos, G.A., Joly, S., Mallet, M., Vallet, I.: RSM-RANS flow prediction in aircraft engine intake double-S-shaped duct. *J. Aircr.* **47**, 1368–1381 (2010)
10. Delot, A.L., Scharnhorst, R.K.: A comparison of several CFD Codes with experimental data in a diffusing S-duct. In: Proceedings of 49th AIAA/ASME/SAE/ASEE Joint Propulsion Conference, AIAA Paper 2013-3796 (2013)
11. Kozulovic, D., Röber, T.: Modelling the streamline curvature effects in turbomachinery flows. In: Proceedings of ASME Turbo Expo 2006: Power for Land, Sea and Air, Barcelona, Spain, GT2006-90265 (2006)
12. Menter, F.R., Kuntz, M., Langtry, R.: Ten Years of Industrial Experience with the SST Turbulence Model. Begell (2003)
13. Hellsten, A.K.: New advanced k- $\omega$  turbulence model for high-lift aerodynamics. *AIAA J.* **43**(9), 1857–1869 (2005)
14. Kächele, T., Niehuis, R., Schneider, T.: Study on efficient full annulus URANS computations of an intake compressor configuration. In: Proceedings of 30th Congress of the International Council of the Aeronautical Sciences, Daejeon, Korea, ICAS2016-0548 (2016)

New Results in Numerical and Experimental Fluid  
Mechanics XI

Contributions to the 20th STAB/DGLR Symposium

Braunschweig, Germany, 2016

Dillmann, A.; Heller, G.; Krämer, E.; Wagner, C.;

Bansmer, S.; Radespiel, R.; Semaan, R. (Eds.)

2018, XV, 767 p. 465 illus., 360 illus. in color.,

Hardcover

ISBN: 978-3-319-64518-6